Showcasing research from Professor Nishihara's laboratory, Department of Chemistry, School of Science, The University of Tokyo, Tokyo, Japan.

Interfacial transmetallation synthesis of a platinadithiolene nanosheet as a potential 2D topological insulator

Transmetallation of a dibutyltin-protected benzenehexathiol ligand with Pt^{2+} in the presence of dioxygen at the liquid-liquid interface affords multi-layer platinadithiolene (PtDT) nanosheets stacked in a half-way slipped hexagonal configuration. This PtDT is insulating and its theoretical band structure exhibits a band gap at the Fermi level, and a Dirac gap, indicating the possibility of 2D topological insulation at room temperature. Conductivity of PtDT is increased drastically by oxidation with iodine. The PtDT nanosheet exhibits high electrocatalytic activity for the hydrogen evolution reaction.

ROYAL SOCIETY OF CHEMISTRY | Celebrating IYPT 2019

rsc.li/chemical-science

Registered charity number: 207890

Interfacial transmetallation synthesis of a platinadithiolene nanosheet as a potential 2D topological insulator†

Tigmansu Pal, [a] Shotaro Doi,[b] Hiroaki Maeda,[a] Keisuke Wada,[a] Choon Meng Tan, [a] Naoya Fukui,[a] Ryota Sakamoto, [a] Shinji Tsuneyuki,[b] Sono Sasaki[cd] and Hiroshi Nishihara [*a]

The construction of two-dimensional metal complex materials is fascinating because of the structural and functional diversity of these materials. Previously, we have reported the synthesis of electroconductive nickelladithiolene (NiDT) and palladadithiolene (PdDT) nanosheets using benzenehexathiol (BHT). Down the group from Ni, Pd to Pt, there is a distinct positive shift in the reduction potential; as a result, it becomes synthetically more challenging to stabilize Pt^{2+} than to form metallic Pt(0) in the presence of BHT as a reducing agent. Herein, a novel synthetic strategy for the preparation of platinadithiolene nanosheet (PtDT) using a dibutyltin-protected BHT ligand is reported, leading to transmetallation in the presence of dioxygen. Both free-standing stacked sheets and atomic layer sheets were obtained and characterized by microscopic techniques such as AFM, SEM, and TEM. To study the morphology of the sheets and determine their charge neutrality, X-ray photoelectron (XP) and infrared (IR) spectroscopic techniques were used. Powder X-ray diffraction analysis of the multilayer PtDT indicates a half-way slipped hexagonal configuration in the $P\bar{3}1m$ space group. The band structure of this PtDT exhibits a band gap at the Fermi level, which is different from that of NiDT in the staggered configuration, and a Dirac gap, indicating the possibility of 2D topological insulation at room temperature. PtDT is insulating but chemically activated by oxidation with I_2 to increase the conductivity by more than 10^6 folds up to 0.39 S cm^{-1}. The MDT sheets exhibit electrocatalytic activity for the hydrogen evolution reaction, and the activity order is NiDT < PdDT < PtDT.

Introduction

Last two decades have experienced the rise of 2D materials because of their interesting physics; since then, graphene,[1] being inappropriate for application in semiconductor-based devices due to its zero band gap,[2] has sustained and opened a broad window of research in the discovery of other 2D-layered[3] intrinsic non-zero gapped semiconducting materials such as transition metal chalcogenides,[4] hydroxides,[5] carbides,[6] graphdiynes,[7] and other compounds (such as silicene, germanene, phosphorene, *etc.*) of the graphene family,[4] which are primarily inorganic materials. These inorganic 2D materials have gained

significant attention for application in electronics,[4] photonics,[8] spintronics,[9,10] optoelectronics,[8,10,11] valleytronics,[12] and magnetism.[10,13–16] The growing field of materials science desires functionalization and tunability of these 2D materials to improve their physical[17] properties based on their band structure electronics.[2,4]

Regarding the functionalization of 2D materials, the organic molecule-based bottom-up synthetic method is more attractive as it features a significant control over the form (symmetry) and composition (molecular parts) of the desired 2D framework, leading to the formation of delocalized isostructural inorganic lattices with tunable functionalities; hence, strategic ligand design and metal combinations under ambient conditions can lead to the generation of a family of 2D metal complex materials, such as coordination nanosheets (CONASHs),[18,19] having various functionalities.

With respect to metal–ligand combinations, non-innocent dithiols can be the key building blocks of these frameworks as far as electronics is concerned. We have synthesized a bis(dithiolato)nickel (NiDT) nanosheet by a coordination reaction between Ni(II) ion and benzenehexathiol (BHT) at the gas–liquid or liquid–liquid interface and shown that change in the

[a]Department of Chemistry, School of Science, The University of Tokyo, 7-3-1 Hongo, Bunkyo-ku, Tokyo, 113-0033, Japan. E-mail: nisihara@chem.s.u-tokyo.ac.jp

[b]Department of Physics, School of Science, The University of Tokyo, 7-3-1 Hongo, Bunkyo-ku, Tokyo, 113-0033, Japan

[c]Faculty of Fibre Science and Engineering, Kyoto Institute of Technology, Matsugasaki Hashikami-cho 1, Sakyo-ku, Kyoto, 606-8585, Japan

[d]RIKEN SPring-8 Centre, Kouto 1-1-1, Sayo-cho, Sayo-gun, Hyogo, 679-5148, Japan

† Electronic supplementary information (ESI) available. See DOI: 10.1039/c9sc01144g

oxidation state of NiDT is a function of conductivity (up to 160 S cm^{-1}).[20,21] Liu et al. have indicated that the NiDT nanosheet with a direct band gap may be an organic topological insulator (TI),[22] a field presently dominated by inorganic materials. It has also been formulated that spin–orbit coupling (SOC) plays a vital role in spin polarization (or spin-momentum locking) as heavier elements tend to increase the spin–orbit gap by splitting the topmost valence band such that the SOC is sufficiently strong to invert this insulating gap in the case of TIs. We have also reported a synthetic strategy for a palladium analogue (PdDT).[23] Marinescu et al. have reported efficient hydrogen evolution[24–27] from water using a Co analogue. In fact, the copper benzenehexathiol (CuBHT) complex nanosheet has a different mode of coordination of Cu as compared to that of Ni in NiDT; this leads to the alteration of intrinsic electronics and thus superconductivity.[28–30]

In the present study, we have extended the metalladithiolene family to platinum analogues considering its importance because of the heavy-atom effect from the SOC as far as TIs are concerned; considering the difficulties in the synthesis of PdDT nanosheets,[23] the synthesis of bis(dithiolato)platinum (PtDT) nanosheet is more challenging because BHT reduces the platinum salt, which has a stronger oxidizing nature. Previously, HTT-Pt has been reported, where the framework had a triphenylene hexathiol core;[31] however, thin film preparations of these 2D layered material have not been noted. Herein, we report novel bottom-up synthetic strategies for free-standing 2D π-conjugated monolayer and multilayer PtDT nanosheets at the liquid–liquid and gas–liquid interfaces by transmetallation. In addition to synthesis, we report the band structure studies, conductivity of I$_2$-doped nanosheets and excellent electrocatalytic activities of d^8 metalladithiolene nanosheets for the hydrogen evolution reaction (HER).

Results and discussion

Synthesis of SnPtDT and PtDT

For the synthesis of PtDT nanosheets, we initially employed two strategies: the reaction of BHT with K$_2$PtCl$_4$ (similar to the case of NiDT) and the addition of the oxidizing agent K$_3$[Fe(CN)$_6$] in the previous scheme (similar to the case of PdDT) (as shown in the ESI Fig. S1†). Both reactions resulted in the formation of a thin sediment of black powder containing Pt(0) at the junction of the pair of liquids (Fig. S2†); this observation could be explained by the higher positive reduction potential of Pt^{2+} as compared to those of Ni^{2+} and Pd^{2+}. To control the redox potential of BHT to stabilize Pt^{2+} and solubility in organic solvents, we employed a di-n-butyltin-protected benzene hexathiolate, called SnBHT, in this study. BHT was stoichiometrically reacted with di-n-butyltin(iv) dichloride to form SnBHT (Scheme 1A, Fig. S3 and S4†).

The interfacial synthesis of PtDT was carried out (Scheme 1B) using SnBHT to solve the crucial problem of BHT being sparingly soluble in organic solvents; the layering of CH$_2$Cl$_2$ containing SnBHT and aqueous K$_2$PtCl$_4$ was performed (Scheme 1C) in air. After this, the abovementioned dispersion was allowed to stand for 1 day, and a very thin film (called as SnPtDT) was observed at the junction of the two liquids (Fig. S5†). The free-standing SnPtDT-stacked sheet was mounted on the hexamethyldisilazane (HMDS)-modified Si(100) substrate.

The optical microscopy (OM), transmission electron microscopy (TEM) and atomic force microscopy (AFM) images
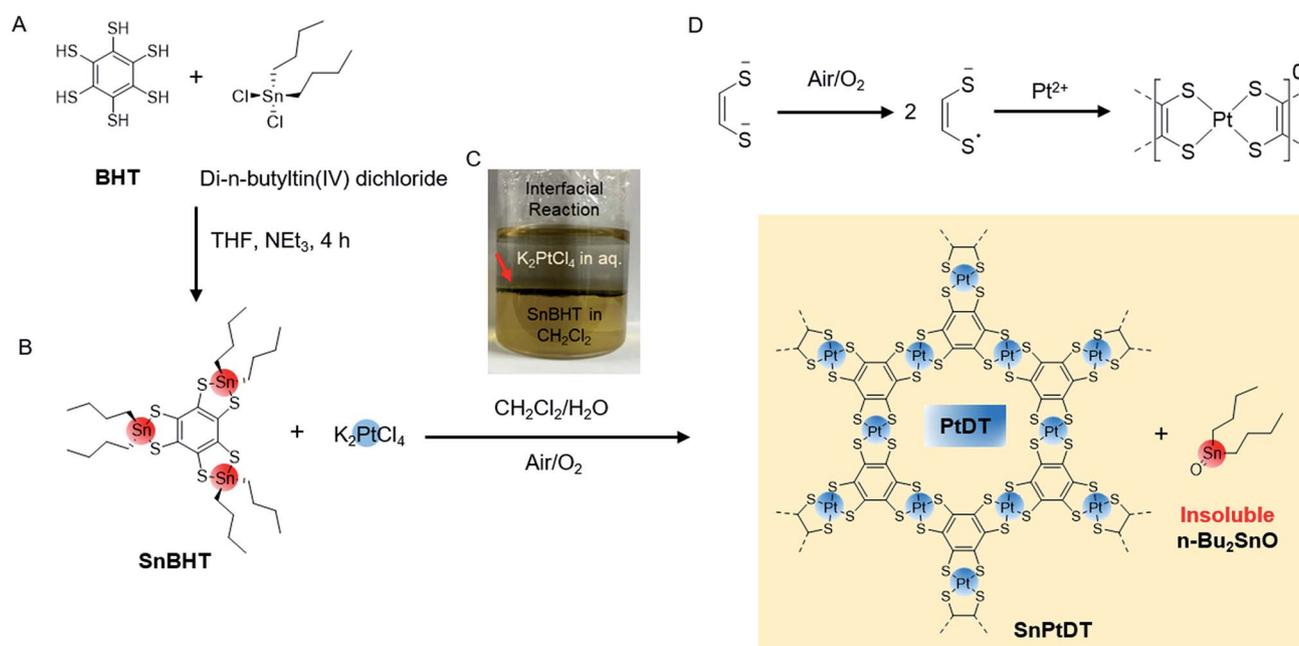
Scheme 1 Synthesis of SnBHT and SnPtDT. (A) Schematic of the synthesis of the protected BHT. (B) Schematic of the synthesis of PtDT containing Bu$_2$SnO (SnPtDT). (C) An optical image of the experimental setup. (D) Mechanism of air oxidation in the dithiolene platinum complex reaction for nanosheet formation.

show a sheet-like morphology (Fig. S6a–d†), with a number of folds resulting in curled edges having random distribution of grains with the average sizes of 60–70 nm over the domain. The particle-like structure was prevalent in as thin as 3 nm sheets, which proves the formation of particles along with the 2D coordination structure PtDT (Fig. S9†). They are possibly metallic Pt(0); however, this possibility is overruled as the XPS spectrum shows the absence of metallic Pt(0) (Fig. S7a†), which is generally shifted to lower values (71.0 eV for Pt $4f_{7/2}$) as compared to Pt^{2+}. XPS reveals the existence of elements at the ratio Pt : S : Sn = 1 : 4.4 : 0.2 (Fig. S8†) and the assignable peaks at 72.5 and 75.7 eV, with well separated spin–orbit components ($\Delta_{Pt} = 3.2$ eV) having the intensity of 4 : 3 for Pt $4f_{7/2}$ and Pt $4f_{5/2}$, respectively (Fig. S7a†), that are similar to those of Pt–S-bonded complexes.[32,33] The formal charge of the $[PtS_4]$ motif is 0, which is reflected in the binding energy of the S atom and determined by the deconvolution of the S 2s envelope at 227.2 and 232.2 eV (Fig. S7c†) originating from the one-electron oxidation of each dithiolene unit (Scheme 1D) and the shake-up peak, respectively.[34,35] The peak shift of S 2s from 226.2 to 227.2 eV confirms the change in the bonding moiety of S from Sn to Pt, whereas the 0.6 eV higher binding energy shift is observed for both Sn $3d_{3/2}$ and $3d_{5/2}$ from SnBHT to SnPtDT (Fig. S7b and d†). The formation of di-n-butyltin(IV) oxide (Bu_2SnO) occurs by the di-hydroxylation of di-n-butyltin(IV) dichloride (which is formed

after the transmetallation reaction) followed by dehydration (Fig. S6e†). The change in the Sn $3d_{5/2}$ and $3d_{3/2}$ position of both SnBHT and SnPtDT confirms the change in the surrounding moiety of Sn^{4+} from two sulfur linkages to one oxide. It can be concluded that the agglomeration of Bu_2SnO (insoluble in any solvents) results in the formation of a grain-like morphology on the sheet.

Physical separation of the two insoluble solids Bu_2SnO and the PtDT polymer is difficult by methods such as washing with solvents, sonication etc.; therefore, chemical separation is performed by treating the SnPtDT sheet mounted on the HMDS-modified Si(100) substrate with a concentrated acetic acid solution to promote the ligand exchange reaction[36] (Fig. S6e and f†). The treated sheet is called as PtDT.

The TEM and OM images show a folded sheet-like morphology of PtDT (Fig. 1A and S6g†). The AFM images show thin films mounted on the HMDS-modified Si(100) substrate of the large lateral domain of 400–500 μm² with an approximately 4–9 nm height (approximately 9–21 layers with respect to the interlayer distance of 4.19 Å (vide infra in crystal structure)), as shown in Fig. 1H. Note that neither metallic Pt(0) nor the islands of insoluble agglomerates of Bu_2SnO are observed. The ligand exchange reaction was successfully accomplished at the solid–liquid interface. Furthermore, via selected area electron diffraction (SAED), a hexagonal
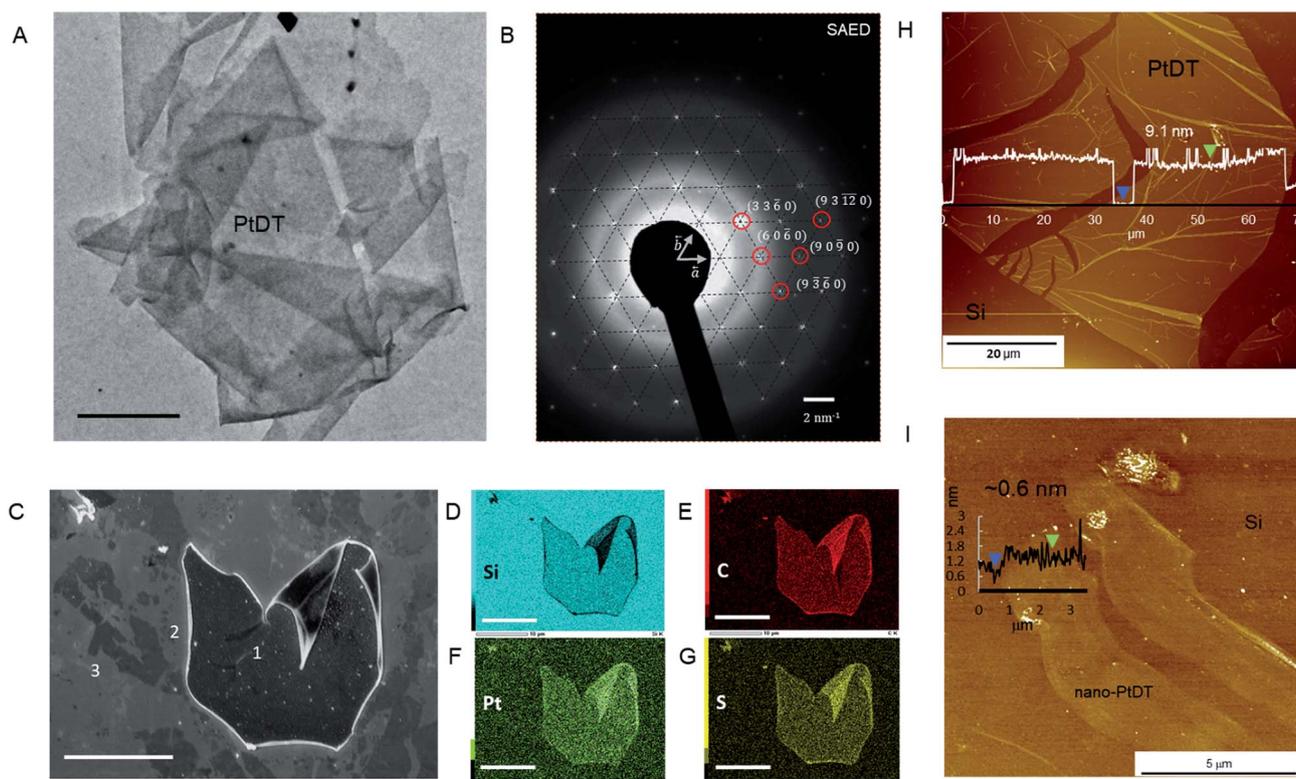

Fig. 1 Microscopic analysis of PtDT. (A) A TEM image showing thin folded PtDT without any agglomerate of Bu_2SnO (scale = 500 nm); (B) SAED pattern of PtDT from (A). (C) An SEM image of PtDT showing different thicknesses of PtDT scattered on the Si surface are marked as 1, 2 and 3; (D–G) EDS of the same area as shown in (C), (scale = 10 μm). (H) An AFM image showing the very large domain 30–60 μm of thickness of 9.1 nm. (I) An AFM image of nano-PtDT showing the large domain size of 10 × 3 μm² of one atomic thick layer of 0.6 nm, (colored markers show corresponding height profiles).

diffraction pattern was obtained, as shown in Fig. 1B, implying that the skeleton of the framework had a hexagonal lattice with the in-plane cell length of 1.57 ± 0.07 nm. The plane indices shown in Fig. 1B are consistent with the modelled kagome lattice.

The IR spectrum of PtDT shows disappearance of the sp^3 C–H stretching peaks of the di-*n*-butyl groups at 2955, 2920 and 2852 cm^{-1} after the ligand exchange reaction as the more insoluble Bu_2SnO solubilizes with di-*n*-butyltin(IV) diacetate (Fig. S10†). Moreover, the broad C–S$^{\cdot}$ stretching peak[37] is observed at 1086 cm^{-1} for PtDT. XPS analysis reveals the existence of the elements S and Pt at the ratio of Pt : S = 1 : 3.8, which is similar to SnPtDT, and the disappearance of the Sn peaks marks the success of the ligand exchange reaction (Fig. S12†). The formal charge of $[PtS_4]^n$ remains zero ($n = 0$), as reflected from the binding energies of the S and Pt atoms, which are similar to those of SnPtDT (Fig. S11†). As a result, the sheet survived decomposition during treatment with concentrated acetic acid. Field-emission scanning electron microscopy (FE-SEM) and elemental mapping images obtained by SEM-energy dispersive spectroscopy (SEM-EDS) show uniform distribution of Pt, S and C in the thick PtDT nanosheet, as shown in marked area 1 (Fig. 1C–G); this confirms compositional homogeneity. There are various thinner nanosheets around 1, which get exfoliated while transferring PtDT on the HMDS-modified Si(100) substrate.

Thinner films can be achieved *via* gas–liquid interfacial reactions (Fig. S13†) by spreading a measured amount of ligand dissolved in benzene on the surface of aqueous solution containing metal ion (K_2PtCl_4 0.5 mM). The thickness of the nanosheet (in nm) can be controlled by the concentration of the ligand (typically 7.3 μM SnBHT in benzene), the time of reaction and the surface coverage (30–70%), which was calculated using the space-filling model (Fig. S14†). Nano-PtDT was deposited on a clean HMDS-modified Si(100) substrate using the Langmuir–Schaefer (LS) method. A 2D sheet-like morphology with the thickness of 0.6 nm can be seen *via* AFM (distinct from that of the bare Si in the AFM topography), which is supposedly one single layer of the PtDT nanosheet (Fig. 1I).

Crystal structure

Unlike the previously reported NiDT, CoDT or Cu-BHT nanosheets, PtDT has a different stacking pattern, deduced by comparing the experimental and simulated PXRD spectra shown in Fig. 2A. PtDT is oriented in an A–B stacking pattern in the $P\bar{3}1m$ space group with the lattice parameters $a = b = 15.01$ Å (in agreement with the SAED patterns) and $c = 8.39$ Å. This structure is a half-way slipped hexagonal arrangement having the interlayer distance of 4.19 Å, as shown in Fig. 2B and E. The obtained PXRD structure was also tried to fit with the staggered and eclipsed pattern (Fig. S15†); however, we selected the slipped hexagonal pattern for a better fit from the rest of the combinations (as shown in Fig. 2A). Furthermore, this structure was theoretically optimized prior to band structure calculations. The layers that slipped resulted in two different Pt-atom positions. A single pore in the A layer consists of six $[Pt(II)C_4S_4]^0$ motifs; out of these, four Pt-atoms are eclipsed to four Pt-atoms from two adjacent pores of the B layer, marked by solid yellow dots in Fig. 2E; consequently, a chain of the eclipsed Pt-atoms runs through the ABAB stack and can be seen in Fig. 2D (marked in blue box). The remaining two Pt-atoms
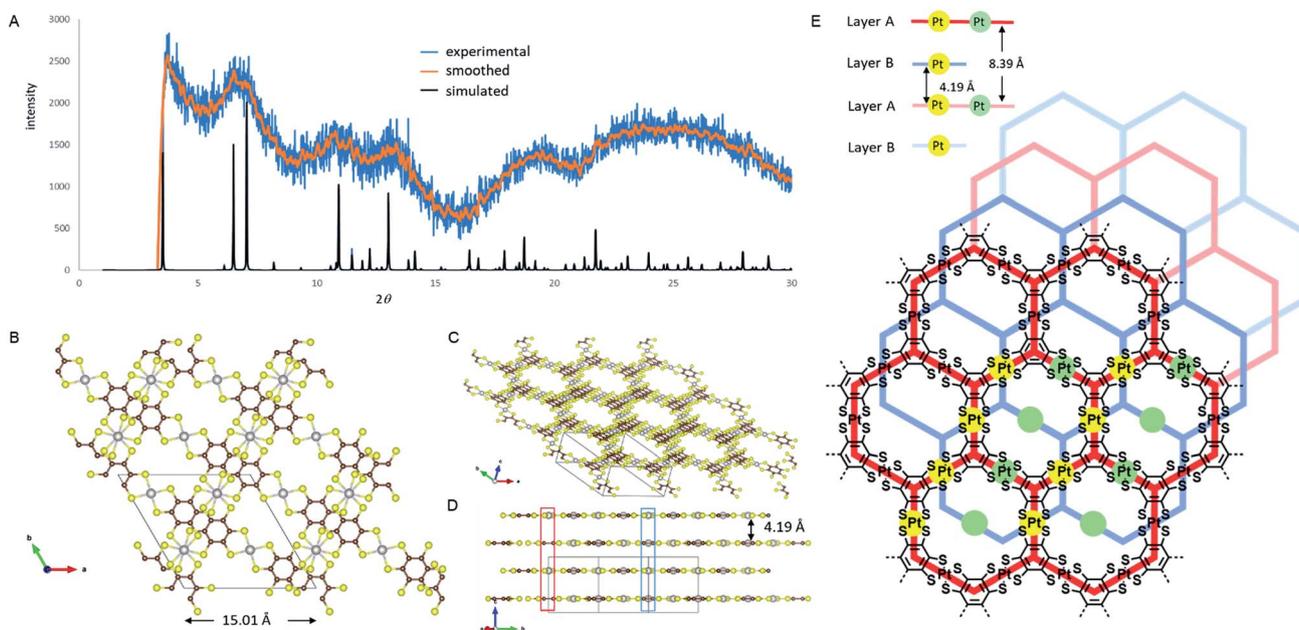

Fig. 2 Crystal structure of PtDT. (A) Comparison of experimental and simulated slipped hexagonal PXRD plot. (B) Longitudinal view along the *c*-axis of PtDT. (C) Tilted view through (111) axis of the stacked PtDT sheet, showing the formation of unidirectional hexagonal pore. (D) Lateral view along the *a*-axis of PtDT. (E) Illustrative representation of AB slipped hexagonal layers of PtDT (considering red and blue as the A and B layer, respectively); (inset) illustrative sideview position of two different Pt-atom centers in the ABAB layers.

of either the A or B layer are eclipsed to two Pt atoms of the alternate A or B layer, respectively, as shown in Fig. 2D and E (marked in red box and green dots) in an alternating AA or BB repeating fashion in the ABAB stacking. The Pt–Pt distance is 4.19 Å and 8.39 Å in the AB and AA layers, respectively. Thus, the halfway slipped hexagonal lattice forms a unidirectional pore and can be viewed through the (111) axis, as shown in Fig. 2C. Surprisingly, the PtDT sheet neither has any π–π interactions as the benzene rings are misoriented nor any metal–metal interactions between layers.

Oxidation and conductivity

Both the pelletized and sheet (thickness < 20 nm) PtDT showed no significant two-probe conductivity, *i.e.* the resistance of the material was more than 10^9 Ω order (10^{-7} S cm^{-1}). This lower conductivity when compared with that of NiDT (160 S cm^{-1}) is reasonable based on the band structures, showing the existence of a band gap for PtDT. The complex nanosheet mounted on the Si/SiO$_2$ substrate was treated with an iodine-CH$_2$Cl$_2$ solution for 12 hours to oxidize some bis(-dithiolato)platinum complexes, and the treated sheets are named as PtDT-I. The XPS spectra of the Pt 4f peaks were deconvoluted into the two different oxidation states of Pt(II) and Pt(IV) (Fig. S16†). The peaks at 73.7 and 77.5 eV for Pt 4f$_{7/2}$ and Pt 4f$_{5/2}$, respectively, were assigned to the +2 cationic form of the complex [PtS$_4$] moiety with I$^-$ acting as a counter anion at 618.7 eV along with elemental iodine in the pores.[32,33,38] Around 8.6–13.2% of the neutral complexes ([PtS$_4$C$_4$]^0) were oxidized to [PtS$_4$C$_4$I$_2$]. The position of iodide is ambiguous as it is possible for iodine to attach to Pt at the axial position or remain as a free ionic pair to the oxidized complex.[39] Raman spectra of PtDT and PtDT-I are identical, proving that there is no change in the vibrational modes (Fig. S17d†). Moreover, the AFM images show no change in the height profile of the nanosheet (Fig. S17b, c and e†). The electrical conductivity measurements were carried out using pelletized sheets. In the four-probe configuration, PtDT-I showed linear current voltage characteristics (Fig. S18†). The conductivity increased drastically to 0.39 S cm^{-1} as compared to that of PtDT. This is consistent with the previously reported I$_2$ activation of the Pt-dithiolene-based coordination polymer.[31]

Electronic structure calculations

We performed electronic structure calculations for PtDT within the framework of the density functional theory (DFT) using the Vienna ab initio simulation package (VASP) software[40] with the projector augmented wave (PAW) method.[41,42] The self-consistent field calculations were carried out with the exchange–correlation energy functional within the generalized gradient approximation (GGA) parametrized by Perdew *et al.*,[43] where we employed the plane-wave cut-off energy of 400 eV and $5 \times 5 \times 10$ Γ-centered k-point mesh for the Brillouin zone integration. Relativistic effects including the SOC were taken into account.

Fig. 3B shows the band structure of PtDT for the 3D multilayer stacked slipped structure with the lattice parameters deduced in the present study ($a = b = 15.01$ Å and $c = 8.39$ Å) along the high-symmetry line in the Brillouin zone in Fig. 3A. Although the half-metallicity of a ferromagnetic kagome spin lattice with the Curie temperature of 212 K has been predicted for 2D MnDT,[44] where the Mn d states are spin-polarized as $S = 3/2$, we have obtained only a spin-unpolarized state. The size of the red dots indicates the weight of the Pt d states to the total states. Energy bands that dominantly comprise the Pt d states are found in the range lower than *ca.* −0.5 eV *versus* the Fermi level, resulting in the almost fully occupied Pt d states without spin polarization. Although the band structure appears as that
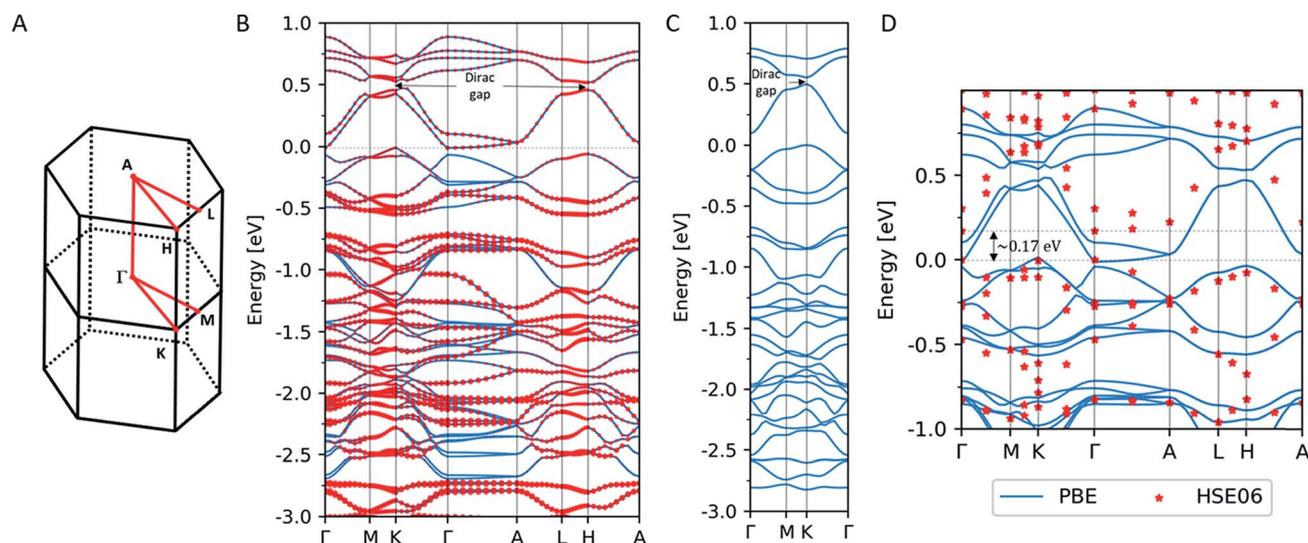

Fig. 3 The band structure of PtDT. (A) The first Brillouin zone and high-symmetry k-points, (B) the 3D stacked slipped lattice by the PBE, (C) the 2D single sheet by the PBE, and (D) the 3D stacked slipped lattice by the HSE06 hybrid functional. The origins of the energy levels are fixed to the VBM.

of an indirect semiconductor, the conduction band minimum (CBM) at the Γ-point is slightly lower than the valence band maximum (VBM) at the K point.

As is well-known, DFT calculations within GGA tend to underestimate the width of the band gaps as compared to the experimental calculations. Thus, we performed band calculations using the HSE06 hybrid functional[45–47] at a limited number of k-points. Fig. 3D shows the band structure of the 3D multilayer stacked slipped PtDT obtained by the HSE06 functional, where solid lines indicate the band structure obtained by PBE and red dots are the corresponding energy levels obtained by the HSE06 functional. We confirmed the opening of a band gap of $\sim$0.17 eV between the CBM and the VBM, in harmony with the conductivity measurement.

In Fig. 3B, another band gap with the width of $\sim$0.074 eV is found at the K-point around $\sim$0.5 eV above the Fermi level, where the SOC opens up a gap at a Dirac point, as indicates for the 2D NiDT;[22] a notable difference is that the stronger SOC of Pt induces a wider band gap as compared to the width of $\sim$0.001 eV for the 2D NiDT. Fig. 3C shows the band structure of the 2D single layer PtDT sheet, where the lattice parameters $a = b = 15.01$ Å are set to the values for the 3D slipped lattice, and a vacuum layer with the thickness of 20.0 Å separates the 2D sheets. We confirmed that there is an indirect band gap of $\sim$0.095 eV around the Fermi level similar to that in the 2D NiDT sheet; however, at the K-point, a wider gap of $\sim$0.054 eV is induced. In the 3D slipped lattice, the 2D character of the band structure is retained since the electronic interaction is small between the adjacent A and B layers. The Dirac gap of 0.054 eV is wider than that for NiDT,[22] 0.016 eV; this suggests that PtDT can be a 2D topological insulator at room temperature.

Hydrogen evolution reaction (HER) catalyst

Coordination nanosheets composed of bis(dithiolato)metal (metal = Ni and Co) have been reported to act as efficient electrocatalysts for the HER.[24–27,48,49] In this study, the MDT sheets (M = Ni,[20] Pd,[23] Pt) were mounted on HOPG to investigate their catalytic activities for the HER in both pH 7 and pH 1.3 H_2SO_4 solutions, as shown in Fig. 4. The onset potentials at pH 1.3 in the case of NiDT, PdDT, PtDT and bare HOPG are found to be at −0.18, −0.08, −0.03 and −0.54 V $vs.$ RHE, respectively. On the other hand, the onset potential values at pH 7 are −0.46, −0.42, −0.10, and −0.78 V $vs.$ RHE. A higher positive onset potential refers to a low-energy catalytic process. Thus, the electrocatalytic activity for the HER increases in the order of NiDT < PdDT < PtDT; this is in fact self-explanatory due to the pronounced catalytic activity of noble metals.

Concluding remarks

In summary, a novel synthetic strategy for platinum analogs of previously reported layered metalladithiolene (Ni and Pd) was successfully achieved. This strategy is unique and establishes an important synthetic route for the use of metals with higher reduction potential; to the best of our knowledge, herein, the construction of nanosheets via transmetallation using air-stable
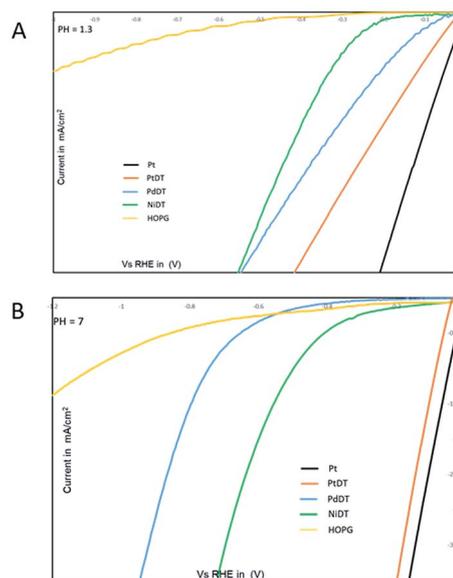

Fig. 4 I−V curves of MDT (M = Ni, Pd, Pt) (A) in a pH 1.3 H_2SO_4 solution; scan rate, 100 mV s^{-1} and (B) in a pH 7 in 0.1 M KCl solution; scan rate, 100 mV s^{-1}.

SnBHT has been reported for the first time. Pure, clean and large domains of PtDT were obtained by ligand-exchange reactions to remove solid by-product. Stacked sheets and sheets as thin as a monolayer were synthetically prepared and characterized by different microscopic and spectroscopic techniques. To determine the charge neutrality of the sheet, XPS and IR spectroscopies were performed. PXRD analysis of multilayer PtDT indicates a half-way slipped hexagonal configuration. Band structure exhibits the existence of a band gap at the Fermi level and a Dirac gap, indicating the possibility of 2D topological insulation. We are currently carrying out a study to obtain the experimental evidence of direct observation of a band structure using a large crystalline single domain PtDT by angle-resolved photoemission spectroscopy (ARPES). Lastly, we have shown a post-electronic modification of the nanosheet by changing the Fermi level of the sheet. The PtDT nanosheets were chemically activated by oxidation with I_2 to increase the conductivity by 10^6 folds. The NiDT, PdDT, and PtDT nanosheets catalyze the electrochemical HER. This key finding in the family of coordination nanosheets broadens the use of more viable combinations in the bottom-up approach for thin film fabrication and electronics, resulting in better surface science and nanodevices.

Experimental

Methods and materials

K_2PtCl_4 was purchased from Kanto Chemical Co., Inc. n-Bu$_2$SnCl$_2$ was received from Wako Pure Chemical Industries, Ltd. Water was purified using the Milli-Q purification system (Merck KGaA). Benzenehexathiol (BHT) was synthesized according to the literature.[51] FE-SEM images were collected using a JEOL JSM-7400FNT equipped with an EDS analyzer (JEOL EX-2300). TEM images were recorded at 75 kV using a Hitachi HF-2000 equipped with an AMT-

CCD camera. The TEM samples were prepared by depositing PtDT on a carbon film supported by a copper grid using an ethanol suspension. IR(ATR) spectra were recorded using a Jasco FT/IR-6100 at room temperature under vacuum. XPS data were obtained using PHI 5000 VersaProbe (ULVAC-PHI, INC.). Al Kα (15 kV, 25 W) was used as the X-ray source, and the beam was focused on a 100 μm^2 area. The spectra were analyzed with MultiPak Software and standardized using a C(1s) peak at 284.6 eV. AFM was carried out using an Agilent Technologies 5500 Scanning Probe Microscope under ambient conditions. AFM was performed in the high-amplitude mode (tapping mode), with a silicon cantilever PPP-NCL (Nano World). The Raman spectra were obtained by LabRAM HR Evolution (HORIBA Scientific).

Electrical conductivity data were collected using the standard four electrode method. Both PtDT and PtDT-I (10 mg) were pressed with a pressure of 500 kg cm^{-2} to form self-standing films. These pelletized films were placed on a glass plate and were attached to four gold electrodes using carbon paste (Fujikura Kasei Co., Ltd) as shown in Fig. S16.† The gold electrodes are attached to the copper electrodes using gold paste. A Keithley Model 2450 SourceMeter® source measure unit (SMU) instrument was used for the four probe conductivity measurement.

Substrate preparations

HOPG was purchased from Alliance Biosystems, Inc. (Grade SPI-1 10 × 10 × 2 mm) and cleaved with an adhesive tape just before use. Silicon wafers (P-doped with a concentration of 3 × 10^{18} cm^{-3}) with thermally grown 100 nm-thick SiO_2 were purchased from Yamanaka Semiconductor, and cut into squares (1 × 1 cm). HMDS treatment was carried out in a Petri dish. A silicon wafer was immersed in an ethanol solution (10 mL) of HMDS (100 μL) for 1 day. After annealing at 130 °C for 2 min, the wafer was rinsed with ethanol and dried *in vacuo*.

Synthesis of SnBHT

In a dry Schlenk flask, BHT (40 mg, 0.18 mmol, 1 equivalent) was taken and Ar was purged for few times. Dry THF was added for about 10 mL with continuous stirring, followed by the addition of NEt_3 (160 μL, 1.116 mmol, 6.2 equiv.), thus forming a pale yellow precipitate. The pale-yellow precipitate was very sensitive to oxygen or air; thus, the precipitate was kept under Ar. To the precipitated mixture, di-*n*-butyltin(IV) dichloride (142 mg, 0.54 mmol, 3.0 equiv.) was added and immediately the precipitate dissolves and forms clear pale yellow solution. The resultant solution was stirred for 4 h and a tin-protected benzenehexathiolate, called as SnBHT, was formed. THF was removed and SnBHT was extracted in hexane to obtain a pale yellow solid. Yield – 85%. SnBHT was characterized by ^1H, ^{13}C NMR spectroscopy, ESI mass spectroscopy, IR spectroscopy. ^1H NMR (400 MHz, $CDCl_3$): 0.908 (t, 3H), 1.372 (sextet, 2H), 1.761–1.633 (m, 4H), ^{13}C NMR (400 MHz, $CDCl_3$): 135.6 (aromatic C), 28.06, 26.99, 21.72, 13.79. HR-ESI-TOF-MS (negative): m/z 998.92; calcd for $C_{30}H_{54}S_6Sn_3Cl$, [L + Cl^-]: 998.929. IR: 2956, 2923 and 2854 cm^{-1} (sp^3 C–H stretching), 1294, 1270 cm^{-1} (C–S stretching).

Synthesis of SnPtDT

Under an argon atmosphere, 1.2–1.5 mg of SnBHT and degassed dichloromethane (10 mL) was added in a N_2 purged glass vial with a diameter of 30 mm, followed by layering with degassed pure water (10 mL) to form a double layer. A degassed aqueous solution (10 mL) containing K_2PtCl_4 (1–2 mM) was then added to the water phase. After waiting for 1 day, SnPtDT emerged at the interface as a thin black solid with a metallic luster. After mounting the sheet on the substrate, it was thoroughly washed with water, acetone, and dichloromethane, and dried in vacuum at 110 °C to afford lustrous black sheets as the substrate.

Synthesis of PtDT and removal of dibutyltin oxide

Under an argon atmosphere, a 10 mm thick bed of anhydrous Na_2SO_4 was made. Later, degassed concentrated acetic acid was taken (15 mL) and added in a N_2 purged glass vial with a diameter of 30 mm. The substrate containing SnPtDT emerged in the acetic acid layer and then rested on top of the bed. After 12 h of standing, the substrate was washed thoroughly in dichloromethane and dried under vacuum at 110 °C to afford black sheets as the substrate.

Synthesis of PtDT-I

Under an air atmosphere, 15 mg of powdered PtDT taken in a vial was added to 15 mL of 0.2 mM of I_2 in CH_2Cl_2. After 12 h of stirring, the mixture was filtered and washed thoroughly with dichloromethane and dried under vacuum at 110 °C to afford a black powder. Similar reaction conditions were used for substrates.

Conflicts of interest

There are no conflicts to declare.

Acknowledgements

Notes and references

1 M. J. Allen, V. C. Tung and R. B. Kaner, *Chem. Rev.*, 2010, **110**, 132–145.

2 X. Xu, C. Liu, Z. Sun, T. Cao, Z. Zhang, E. Wang, Z. Liu and K. Liu, *Chem. Soc. Rev.*, 2018, **47**, 3059–3099.

3   C. Tan, X. Cao, X.-J. Wu, Q. He, J. Yang, X. Zhang, J. Chen, W. Zhao, S. Han, G.-H. Nam, M. Sindoro and H. Zhang, *Chem. Rev.*, 2017, **117**, 6225–6331.

4   Y. Liu, X. Duan, Y. Huang and X. Duan, *Chem. Soc. Rev.*, 2018, **47**, 6388–6409.

5   B. R. Ma and T. Sasaki, *Adv. Mater.*, 2010, **22**, 5082–5104.

6   J. Pang, R. G. Mendes, A. Bachmatiuk, L. Zhao, H. Q. Ta, T. Gemming, H. Liu, Z. Liu and M. H. Rummeli, *Chem. Soc. Rev.*, 2019, **48**, 72–133.

7   R. Sakamoto, N. Fukui, H. Maeda, R. Matsuoka, R. Toyoda and H. Nishihara, *Adv. Mater.*, 2019, DOI: 10.1002/adma.201804211.

8   Q. Bao and K. P. Loh, *ACS Nano*, 2012, **6**, 3677–3694.

9   J. H. Garcia, M. Vila, A. W. Cummings and S. Roche, *Chem. Soc. Rev.*, 2018, **47**, 3359–3379.

10 D. Zhong, K. L. Seyler, X. Linpeng, R. Cheng, N. Sivadas, B. Huang, E. Schmidgall, T. Taniguchi, K. Watanabe, M. A. McGuire, W. Yao, D. Xiao, K.-M. C. Fu and X. Xu, *Sci. Adv.*, 2017, **3**, 1603113.

11 V. W. Brar, M. C. Sherrott and D. Jariwala, *Chem. Soc. Rev.*, 2018, **47**, 6824–6844.

12 K. F. Mak, K. He, J. Shan and T. F. Heinz, *Nat. Nanotechnol.*, 2012, **7**, 494–498.

13 C. Gong, L. Li, Z. Li, H. Ji, A. Stern, Y. Xia, T. Cao, W. Bao, C. Wang, Y. Wang, Z. Q. Qiu, R. J. Cava, S. G. Louie, J. Xia and X. Zhang, *Nature*, 2017, **546**, 265–269.

14 B. Huang, G. Clark, E. N. Moratalla, D. R. Klein, R. Cheng, K. L. Seyler, D. Zhong, E. Schmidgall, M. A. McGuire, D. H. Cobden, W. Yao, D. Xiao, P. J. Herrero and X. Xu, *Nature*, 2017, **546**, 270–273.

15 M. Bonilla, S. Kolekar, Y. Ma, H. C. Diaz, V. Kalappattil, R. Das, T. Eggers, H. R. Gutierrez, M.-H. Phan and M. Batzill, *Nat. Nanotechnol.*, 2018, **13**, 289–293.

16 S. Jiang, J. Shan and K. F. Mak, *Nat. Mater.*, 2018, **17**, 406–410.

17 N. Peimyoo, J. Li, J. Shang, X. Shen, C. Qiu, L. Xie, W. Huang and T. Yu, *ACS Nano*, 2012, **6**, 8878–8886.

18 R. Sakamoto, K. Takada, T. Pal, H. Maeda, T. Kambe and H. Nishihara, *Chem. Commun.*, 2017, **53**, 5781–5801.

19 R. Dong, T. Zhang and X. Feng, *Chem. Rev.*, 2018, **118**, 6189–6235.

20 T. Kambe, R. Sakamoto, K. Hoshiko, K. Takada, M. Miyachi, J. H. Ryu, S. Sasaki, J. Kim, K. Nakazato, M. Takata and H. Nishihara, *J. Am. Chem. Soc.*, 2013, **135**, 2462–2465.

21 T. Kambe, R. Sakamoto, T. Kusamoto, T. Pal, N. Fukui, K. Hoshiko, T. Shimojima, Z. Wang, T. Hirahara, K. Ishizaka, S. Hasegawa, F. Liu and H. Nishihara, *J. Am. Chem. Soc.*, 2014, **136**, 14357–14360.

22 Z. F. Wang, N. Su and F. Liu, *Nano Lett.*, 2013, **13**, 2842–2845.

23 T. Pal, T. Kambe, T. Kusamoto, M. L. Foo, R. Matsuoka, R. Sakamoto and H. Nishihara, *ChemPlusChem*, 2015, **80**, 1255–1258.

24 A. J. Clough, J. W. Yoo, M. H. Mecklenburg and S. C. Marinescu, *J. Am. Chem. Soc.*, 2015, **137**, 118–121.

25 C. A. Downes, A. J. Clough, K. Chen, J. W. Yoo and S. C. Marinescu, *ACS Appl. Mater. Interfaces*, 2018, **10**, 1719–1727.

26 C. A. Downes and S. C. Marinescu, *ChemSusChem*, 2017, **10**, 4374–4392.

27 A. J. Clough, J. M. Skelton, C. A. Downes, A. A. de la Rosa, J. W. Yoo, A. Walsh, B. C. Melot and S. C. Marinescu, *J. Am. Chem. Soc.*, 2017, **139**, 10863–10867.

28 X. Huang, P. Sheng, Z. Tu, F. Zhang, J. Wang, H. Geng, Y. Zou, C. A. Di, Y. Yi, Y. Sun, W. Xu and D. Zhu, *Nat. Commun.*, 2015, **6**, 7408.

29 X. Huang, S. Zhang, L. Liu, L. Yu, G. Chen, W. Xu and D. Zhu, *Angew. Chem., Int. Ed.*, 2018, **57**, 146–150.

30 X. Huang, H. Yao, Y. Cui, W. Hao, J. Zhu, W. Xu and D. Zhu, *ACS Appl. Mater. Interfaces*, 2017, **9**, 40752–40759.

31 J. Cui and Z. Xu, *Chem. Commun.*, 2014, **50**, 3986–3988.

32 J. Dembowski, L. Marosi and M. Essig, *Surf. Sci. Spectra*, 1993, **2**, 133–137.

33 J. Dembowski, L. Marosi and M. Essig, *Surf. Sci. Spectra*, 1993, **2**, 104–108.

34 S. Zhou, K. Ichimura and H. Inokuchi, *J. Mater. Chem.*, 1995, **5**, 1725–1729.

35 S.-G. Liu, Y.-Q. Liu and D.-B. Zhu, *Synth. Met.*, 1997, **89**, 187–191.

36 J. Beckmann, D. Dakternieks, F. S. Kuan and E. R. T. Tiekink, *J. Organomet. Chem.*, 2002, **659**, 73–83.

37 K. Ray, T. Weyhermuller, F. Neese and K. Wieghardt, *Inorg. Chem.*, 2005, **44**, 5345–5360.

38 P. M. A. Sherwood, *J. Chem. Soc., Faraday Trans. 2*, 1976, **72**, 1805–1820.

39 P. Chandrasekaran, A. F. Greene, K. Lillich, S. Capone, J. T. Mague, S. DeBeer and J. P. Donahue, *Inorg. Chem.*, 2014, **53**, 9192–9205.

40 G. Kresse and J. Hafner, *Phys. Rev. B: Condens. Matter Mater. Phys.*, 1993, **47**, 558–561.

41 P. Blöchl, *Phys. Rev. B: Condens. Matter Mater. Phys.*, 1994, **50**, 17953–17979.

42 G. Kresse and D. Joubert, *Phys. Rev. B: Condens. Matter Mater. Phys.*, 1999, **59**, 1758–1775.

43 J. P. Perdew, K. Burke and M. Ernzerhof, *Phys. Rev. Lett.*, 1996, **77**, 3865–3868.

44 M. Zhao, A. Wang and X. Zhang, *Nanoscale*, 2013, **5**, 10404–10408.

45 J. Heyd and G. E. Scuseria, *J. Chem. Phys.*, 2003, **118**, 8207–8215.

46 J. Heyd and G. E. Scuseria, *J. Chem. Phys.*, 2004, **121**, 1187–1192.

47 J. Heyd and G. E. Scuseria, Erratum: "Hybrid functionals based on a screened Coulomb potential", *J. Chem. Phys.*, 2003, **118**, 8207, *J. Chem. Phys.*, 2006, **124**, 219906.

48 R. Dong, M. Pfeffermann, H. Liang, Z. Zheng, X. Zhu, J. Zhang and X. Feng, *Angew. Chem., Int. Ed.*, 2015, **54**, 12058–12063.

49 R. Dong, Z. Zheng, D. C. Tranca, J. Zhang, N. Chandrasekhar, S. Liu, X. Zhuang, G. Seifert and X. Feng, *Chem.–Eur. J.*, 2016, **23**, 2255–2260.

50 K. Kato, R. Hirose, M. Takemoto, S. Ha, J. Kim, M. Higuchi, R. Matsuda, S. Kitagawa and M. Takata, *AIP Conf. Proc.*, 2010, **1234**, 875–878.

51 J. A. Harnisch and R. J. Angelici, *Inorg. Chim. Acta*, 2000, **300–302**, 273–279.